J. Fluid Mech. (2010), *vol.* 655, *pp.* 306–326.
doi:10.1017/S002211201000087X

Transition behaviour of weak turbulent fountains

N. WILLIAMSON[1]†, S. W. ARMFIELD[1] AND WENXIAN LIN[2]

[1]School of Aerospace, Mechanical and Mechatronic Engineering, The University of Sydney, NSW 2006, Australia

[2]School of Engineering & Physical Sciences, James Cook University, Townsville, Queensland 4811, Australia

(Received 30 November 2009; revised 10 February 2010; accepted 10 February 2010; first published online 11 May 2010)

Numerical simulations of fully turbulent weak fountain flow are used to provide direct evidence for the scaling behaviour of fountain flow over the Froude number range $Fr = 0.1-2.1$ and Reynolds number range $Re = 20$–3494. For very weak flow at $Fr < 0.4$, the flow mean penetration height, Z_m, scales with $Z_m/R_0 = A_1 Fr^{2/3} + A_2 Fr^{2/3}$ where R_0 is the source radius. A_1 and A_2 are constants which quantify the separate effects of the radial acceleration of fountain fluid from the source (A_1) and the backpressure from the surrounding intrusion, if present, on the upflow (A_2). The evidence presented in this work suggests that the mechanisms for the two parts in the scaling of Z_m scale with $Fr^{2/3}$. The intrusion behaviour varies with the Reynolds number (Re) but there is no Re affect on the fountain penetration height. For $Re < 250$ the radial intrusion flow is subcritical and has different behaviour. For Fr between 0.4 and 2.1 the effect of source momentum flux increases and the flow structure changes to one where there is a coherent upflow and a cap region where the flow stagnates and then reverses. The two regions have separate scaling behaviour such that the overall height, through this transition range of Froude numbers, can be described by $Z_m/R = C_1 Fr^{2/3} + C_2 Fr^2$, where C_1 and C_2 are constants. Over this transition range the effect of source velocity profile is more significant than the Reynolds number effects and the effect of inlet turbulence is minor.

1. Introduction

Turbulent fountains or negatively buoyant jets occur in many industrial and geophysical flows. Examples include the flow of lava in magma chambers (Campbell & Turner 1989; Bloomfield & Kerr 1998), air-conditioning and heating in large buildings (Baines, Turner & Campbell 1990), replenishment of solar ponds (Lin & Armfield 2000*a*) and volcanic eruptions. The configuration considered here has the direction of buoyancy force directly opposed to the flow direction at the source, so that the upwelling fluid penetrates a distance into the ambient fluid before stagnating and then flowing back directly around itself. This flow is characterized by the Froude number,

$$Fr = \left(\frac{M_0 U_B}{R_0 F_0} \right)^{1/2}, \tag{1.1}$$

† Email address for correspondence: n.williamson@usyd.edu.au

where R_0 is the radius of the source. M_0 and F_0 are the source momentum flux and buoyancy flux defined as

$$M_0 = \int_0^{R_0} 2\pi r(\overline{U}^2 + \overline{U'U'})\,\mathrm{d}r, \quad F_0 = \int_0^{R_0} 2\pi\sigma r\overline{U}\,\mathrm{d}r,$$

where $\overline{U}$ is the local time averaged axial velocity and $\overline{U'U'}$ is the streamwise normal stress, σ is the reduced gravity between the fountain source and the ambient fluid and is defined as $\sigma = g(\rho_0 - \rho_\infty)/\rho_\infty$, with the subscript 0 indicating a quantity at the fountain source and ∞ a property of the ambient fluid. $U_B = Q_0/A_0$ is the bulk velocity at the source with Q_0 and A_0 being the volume flow rate and source cross-sectional area, respectively. The characteristic velocity resulting from (1.1) is $U_0 = (M_0/\pi R_0^2)^{0.5}$ which differs from U_B by a factor depending on the source velocity profile and $\overline{U'U'}$.

In high Froude number flow, where $Fr \gtrsim 3$, the buoyancy forces are weak compared with the source momentum flux and the fountain penetrates a large distance into the ambient fluid. The upflow behaves like a turbulent jet with strong mixing and entrainment of ambient fluid while the downflow behaves more like a dense plume (Baines *et al.* 1990; Bloomfield & Kerr 2000). Both the upflow and downflow continue to develop along their trajectories so the flow never attains self-similarity and the flow statistics vary with axial location and Froude number (Mizushina *et al.* 1982). The steady-state penetration depth Z_m scales as $Z_m \sim M_0^{3/4}/F_0^{1/2}$ (Turner 1966) or in terms of the source Froude number, $Z_m/R_0 = CFr$, where C is a constant of proportionality ranging between 2.1 and 3.06 (Turner 1966; Campbell & Turner 1989; Baines *et al.* 1990; Cresswell & Szczepura 1993; Kaye & Hunt 2006; Williamson *et al.* 2008*b*; Baddour & Zhang 2009). These experimental studies and the analytical work of Kaye & Hunt (2006) suggest that this turbulent flow regime exists for $Fr \gtrsim 3$. Below the tentative lower limit, over the range $Fr \sim 0$–3, the fountain undergoes a transition from buoyancy dominated 'very weak flow' to fully developed free shear flow (Kaye & Hunt 2006). Within this range of $Fr \sim 0$–3 there is considerable variation in flow behaviour, which is the focus of this study. Preliminary work by the present authors, using direct numerical simulation (DNS) of turbulent fountain flow, showed that at $Fr = 0.45$ the flow is contained around the source and no ambient fluid is drawn into the fountain core (Williamson, Armfield & Lin 2008*a*). At $Fr = 2.1$ a weak shear mixing region is established between the inner upflow, the outer downflow and the ambient.

The change in flow behaviour described above is reflected in the scaling relations for fountain height. Zhang & Baddour (1997) suggested two low Froude number scalings for plane turbulent fountains, first proposing $Z_m = f(Q_0, F_0) = CQ_0F_0^{-1/3}$ giving $Z_m/R_0 \sim Fr^{2/3}$, and second suggesting a simple zero entrainment model which results in $Z_m \sim Fr^2$. Zhang & Baddour (1998) performed experiments with round fountains over the range $850 < Re < 12750$ and $0.37 < Fr < 36.2$. For $Fr > 7$ they found the mean maximum penetration height follows $Z_{max}/R_0 = 3.06Fr$ but for $Fr < 7$ it is better represented by $Z_{max}/R_0 = 1.7Fr^{1.3}$.

Lin & Armfield (2000*a*) later used numerical simulations to examine laminar weak fountain flow and found $Z_m/R_0 \sim Fr$ for round fountains over the range $0.2 \leqslant Fr \leqslant 1.0$. In subsequent work they extended this work to $0.0025 \leqslant Fr \leqslant 0.2$, the lowest Froude number range examined till date, finding $Z_m/R_0 \sim Fr^{2/3}$ (Lin & Armfield 2000*b*).

Kaye & Hunt (2006) suggested a three-regime classification of round fountain behaviour, labelling them 'forced' for $Fr > 3$, 'weak' for $1 < Fr < 3$ and 'very weak'

for $Fr < 1$. These labels are adopted in the present work. Using an integral model and assuming entrainment in high Froude number forced fountains is similar to that in non-buoyant jets, they found the well-established result of $Z_m/R_0 \sim Fr$. For weak fountains Kaye & Hunt (2006) used the same model but assumed the influence of entrainment to be small. This approach yielded $Z_m \sim U_0^2/\sigma \equiv M_0^2/Q_0F_0$ or $Z_m/R_0 \sim Fr^2$, indicating direct conversion of flow kinetic energy at the source to potential energy, the same as the second weak model of Zhang & Baddour (1997). For very weak fountains they proposed that the penetration height provides the pressure head to accelerate the flow radially and related the radial outflow of fountain fluid from the nozzle to critical flow over a weir. Using this analogy they found $Z_m/R_0 \sim Fr^{2/3}$ (or $Z_m \sim Q_0/F_0^{1/3}$), the same Froude number scaling obtained by Lin & Armfield (2000*b*) and Zhang & Baddour (1997) but providing for the first time a real physical explanation for the behaviour.

Difficulties in obtaining fully turbulent flow at low Froude number experimentally using the usual saline/fresh water set-up at laboratory scale mean that the details of fully turbulent flow have not yet been reported for very low Froude numbers. Lin & Armfield (2000*a*,*b*) covered a part of this range with their two-dimensional axisymmetric DNS ($0.0025 \leqslant Fr \leqslant 1.0$) however in that work, the Reynolds number was low ($Re = 5$–800). Zhang & Baddour (1998) conducted experiments down to $Fr = 0.37$ and Kaye & Hunt (2006) obtained $Fr \sim 0.2$, but in both cases the Reynolds numbers appear to be low. Mizushina *et al.* (1982) provide high Reynolds number flow statistics for $Fr \approx 5$–260 and Cresswell & Szczepura (1993) for $Fr = 3.16$ flow. The aim of this work is to provide direct evidence for fountain behaviour through the very weak to weak transition range. We approach this problem with DNS of fully turbulent flow over the range $Fr = 0.1$–1.4.

Our numerical model is described in § 2. In § 3 the general flow behaviour is described and in § 4 the rise time and penetration height scaling results are presented. In § 5 a momentum balance of the mean flow is used to illustrate mechanisms governing very weak flow behaviour and quantify the Reynolds number effects. In § 6 the change in flow structure and behaviour through the very weak to weak transition range is examined. The conclusions are summarized in § 7.

2. Numerical formulation

We use DNS to solve the Navier–Stokes equations for incompressible three-dimensional flow and employ the Boussinesq approximation. The non-dimensional continuity, momentum and scalar transport equations are

$$\frac{\partial u_i}{\partial x_i} = 0, \tag{2.1}$$

$$\frac{\partial u_i}{\partial t} + \frac{\partial (u_i u_j)}{\partial x_j} = -\frac{\partial p}{\partial x_i} + \frac{1}{Re}\frac{\partial^2 u_i}{\partial x_j \partial x_j} - \frac{\phi}{Fr^2}, \tag{2.2}$$

$$\frac{\partial \phi}{\partial t} + \frac{\partial (u_j \phi)}{\partial x_j} = \frac{1}{RePr}\frac{\partial^2 \phi}{\partial x_j \partial x_j}, \tag{2.3}$$

where Pr is the Prandtl number, the Reynolds number is defined as $Re = U_0R_0/\nu$ and ν is the kinematic viscosity of the fluid. The velocity (U_i), temperature (θ), pressure (P), time (T) and length (X_i) are made non-dimensional as $u_i = U_i/U_0$, $\phi = (\theta - \theta_\infty)/(\theta_0 - \theta_\infty)$, $p = P/\rho U_0^2$, $t = TU_0/R_0$ and $x_i = X_i/R_0$, respectively.

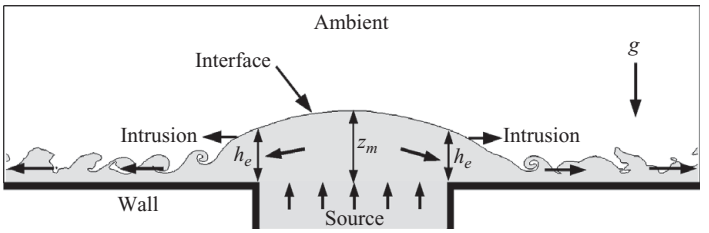

FIGURE 1. Schematic illustration of weak flow configuration.

The discretized governing equations were solved in finite volume form on a non-staggered Cartesian grid. The spatial derivatives were discretized using second-order central finite differences except for the scalar advective term which is discretized nominally by a second-order centred scheme but with the ULTRA-flux limiter applied (Leonard & Mokhtari 1990). We have monitored the effect of the flux limiter carefully and ensured that the grid is sufficiently well resolved such that the limiting only occurs for short periods of time and predominately outside the region of interest in the interface where scalar concentration gradients are very high. The limiter is unfortunately necessary to prevent negative/non-physical temperature regions occurring. The advective terms were advanced in time using the second-order Adams–Bashforth scheme while the viscous terms were advanced using the Crank–Nicolson scheme. A fractional step pressure correction method was used to enforce the divergence-free constraint and update the pressure field (Armfield & Street 1999). The Rhie–Chow momentum interpolation method was used for the cell face velocities in the pressure solver (Armfield & Street 2002). The system of equations was solved with the BI-CGSTAB (van der Vorst 1992) solver with a multi-grid Jacobi pre-conditioner (Brandt 1977).

The computational domain is a rectangular box in which the top and sidewalls are open boundaries. The open boundaries have a zero gradient condition for the velocity and scalar fields and zero second derivative for the pressure correction term. The bottom boundary is no-slip/adiabatic, except for the fountain source located in the centre where the normal velocity and temperature are set as described below.

The configuration in this study is that of a fountain with the source aligned flush with the bottom boundary of the domain, as illustrated in figure 1. The peculiarity of this configuration compared with a re-entrant nozzle configuration commonly used in experimental studies (e.g. Turner 1966; Campbell & Turner 1989; Cresswell & Szczepura 1993; Bloomfield & Kerr 1998) is that the downflowing fluid flows across the lower boundary as a dense intrusion. After a short transient period where the penetration height of the fountain may fluctuate, the fountain reaches a quasi-steady regime where the flow in and immediately around the upflow is established. With a larger domain the intrusion would eventually become viscous and backfill onto the fountain causing a different behaviour to exist. This study is only concerned with the initial transient and quasi-steady regime in this flow configuration within 3–$4R_0$ of the source.

We perform high-Reynolds-number turbulent simulations at $Pr = 0.7$, $Fr = 0.1$–1.4 and $Re = 3494$ ($Re_B = U_B R_0/\nu = 3350$), and examine the Reynolds number effects and the effect of inlet velocity profile.

For the turbulent simulations, the inflow at the fountain source is prescribed as an unsteady boundary condition derived from a separate DNS simulation of turbulent pipe flow at $Re_B = 3350$. The velocity field was recorded across a single cross-section

Fr	Pr	Re	Source	$\frac{\Delta X, Y}{R}, \frac{\Delta Z}{R_0} \times 10^3$	$\frac{L_{x,y}}{R_0}, \frac{L_z}{R_0}$	$N_{x,y}, N_z$	$\frac{Lu_{x,y}}{R_0}, \frac{Lu_z}{R_0}$
0.1	50	20	Uni	47, 8	12, 2	165, 101	2.5, 0.3
0.1	4	250	Uni	47, 8	12, 2	165, 101	2.5, 0.3
0.05–1.0	4	250	Uni	47, 5–8	12, 1–3.5	165, 101	2.5, 0.18–1.4
0.05–1.0	4	250	Par	47, 5–8	12, 1–3.5	165, 101	2.5, 0.18–2.1
0.1	0.7	3494	Pipe	11.5, 7	7, 2	549, 101	2.5, 0.25
0.4	0.7	3494	Pipe	12, 6.8	7, 3.5	517, 133	2.5, 0.25
0.97	0.7	3494	Pipe	13.5, 15	10, 7	389, 197	2.0, 1.7
1.4	0.7	3494	Pipe	15, 13	7, 4	389, 197	2.5, 1.8
2.1	7.0	3494	Pipe	20, 35	40, 30	210, 180	1.2, 4

TABLE 1. Simulation parameters, where source inlet profiles are indicated as: Uni, uniform profile; Pipe, unsteady recording of pipe flow; Par, parabolic inlet profile. ΔX, Y, Z, $L_{x,y,z}$ and $N_{x,y,z}$ give the grid size at the source, the domain size and the number of nodes, respectively.

of a periodic pipe flow simulation at each time step, after the simulation reached a statistically steady state. The resolution of these simulations is 0.5–2 δ_v in the plane cross-section and 3 δ_v in the axial direction, where $\delta_v = \nu\sqrt{\rho/\tau_w}$ and τ_w is the pipe wall shear stress and the pipe length is $2\pi R_0$. The mean flow profile and Reynolds stresses of this simulation compare well with the published values of Fukagata & Kasagi (2002) at $Re_B = 2655$. The mean centreline velocity of the flow is $1.31U_B$ and $U_0/U_B = 1.043$. This recording was then interpolated onto the boundary cell face at the fountain source in the fountain simulation at each time step. This approach ensures a high quality realistic flow, comparable with experimental data, and allows us to quantify the importance of the inlet turbulence on fountain flow behaviour. In all other simulations, the inflow profile is either steady parabolic or uniform. The details of the simulations are given in table 1. The details of a $Fr = 2.1$ simulation presented by Williamson *et al.* (2008*a*) are also given in the table and will be referred to in this work. A regular Cartesian grid is used which is uniform in the horizontal x, y-plane within a distance $Lu_{x,y}$ of the centre of the source. Outside this region the grid is stretched with approximately a 3 % growth rate. The grid is uniform in the axial direction up to Lu_z and stretched at 3 % thereafter. The grid size at the source is approximately $2\delta_v$ for $Fr = 0.1$–1.4, fine enough to resolve the smallest structures in the turbulent pipe flow solution and the fountain flow.

3. Turbulent flow behaviour

The turbulent simulations of $Fr = 0.1$ and $Fr = 0.4$ are in the very weak regime, while the $Fr = 0.97$ simulation is at the transition suggested by Kaye & Hunt (2006) and $Fr = 1.4$ and $Fr = 2.1$ are in the middle of the weak regime. Contours of ϕ and pressure are given in figures 2 and 3 illustrating the flow structure at $Fr = 0.1$ and 0.4. The flow structure at $Fr = 0.97$ and $Fr = 1.4$ is illustrated in figures 4 and 5.

At $Fr = 0.1$ the penetration height is very small compared with the source diameter. Upon entry into the domain the fluid is immediately forced radially into the intrusion. After the initial establishment of the flow, the penetration height is constant with none of the unsteadiness from the source evident. There is negligible mixing or entrainment into either the cap region or the fountain core. The intrusion flow forms around the source and is supplied with a constant steady mass flux from the source. The mixing in the intrusion interface is driven by Kelvin–Helmholtz (K–H) structures

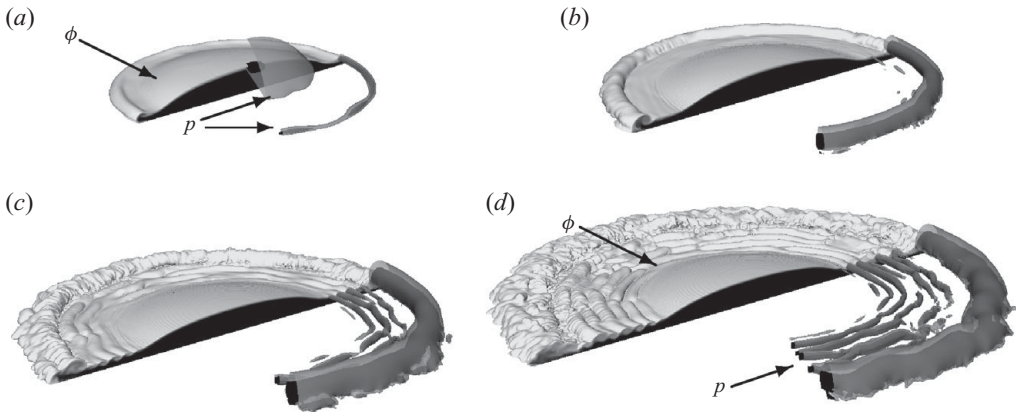

FIGURE 2. Time development of $Fr = 0.1$, $Re = 3494$, $Pr = 0.7$ simulation illustrated with cut-away of ϕ together with isosurfaces of pressure at $p = -3$ and $p = -1.8$. ϕ shading is from $\phi = 1.0$ (black) to $\phi = 0.1$ (light grey). Images (*a–d*) were recorded at $t = 0.35$, 0.5, 0.65 and 0.8, respectively.

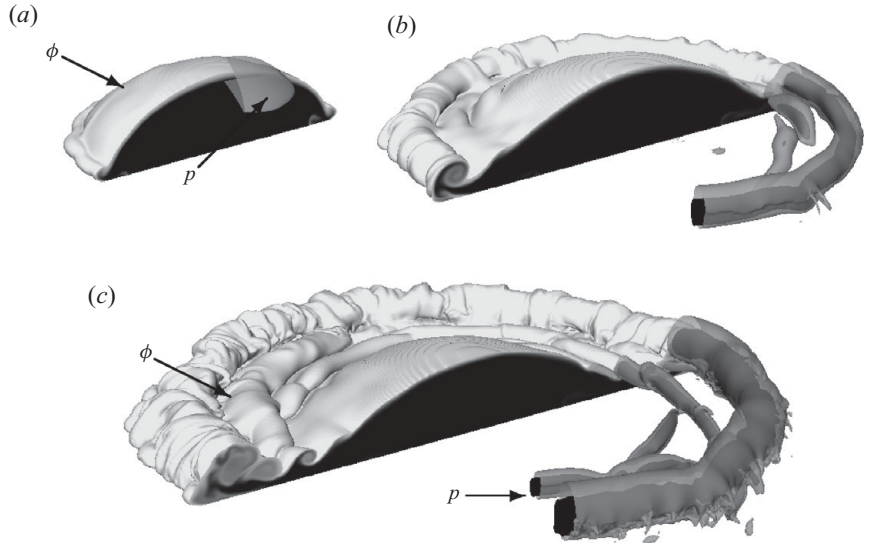

FIGURE 3. Time development of $Fr = 0.4$, $Re = 3494$, $Pr = 0.7$ simulation illustrated with cut-away of ϕ together with isosurfaces of pressure at $p = -1.0$ and $p = -0.49$. ϕ shading is from $\phi = 1.0$ (black) to $\phi = 0.1$ (light grey). Images (*a–c*) were recorded at $t = 0.73$, 1.49 and 2.25, respectively.

which appear after $t = 0.5$. Qualitatively the simulation compares well with the low-Reynolds-number axisymmetric simulations of Lin & Armfield (2000*a*,*b*), except for the mixing in the intrusion. This is examined in § 5. The initial rise and then fall of the fountain front produces a perturbation in the pressure field which is shown in figures 2(*a*) and 3(*a*).

At $Fr = 0.4$, shown in figure 3, the fountain rises to a greater height and the unsteadiness from the inlet boundary condition is evident as deformation of the fountain cap at the interface with the ambient fluid. There is negligible entrainment

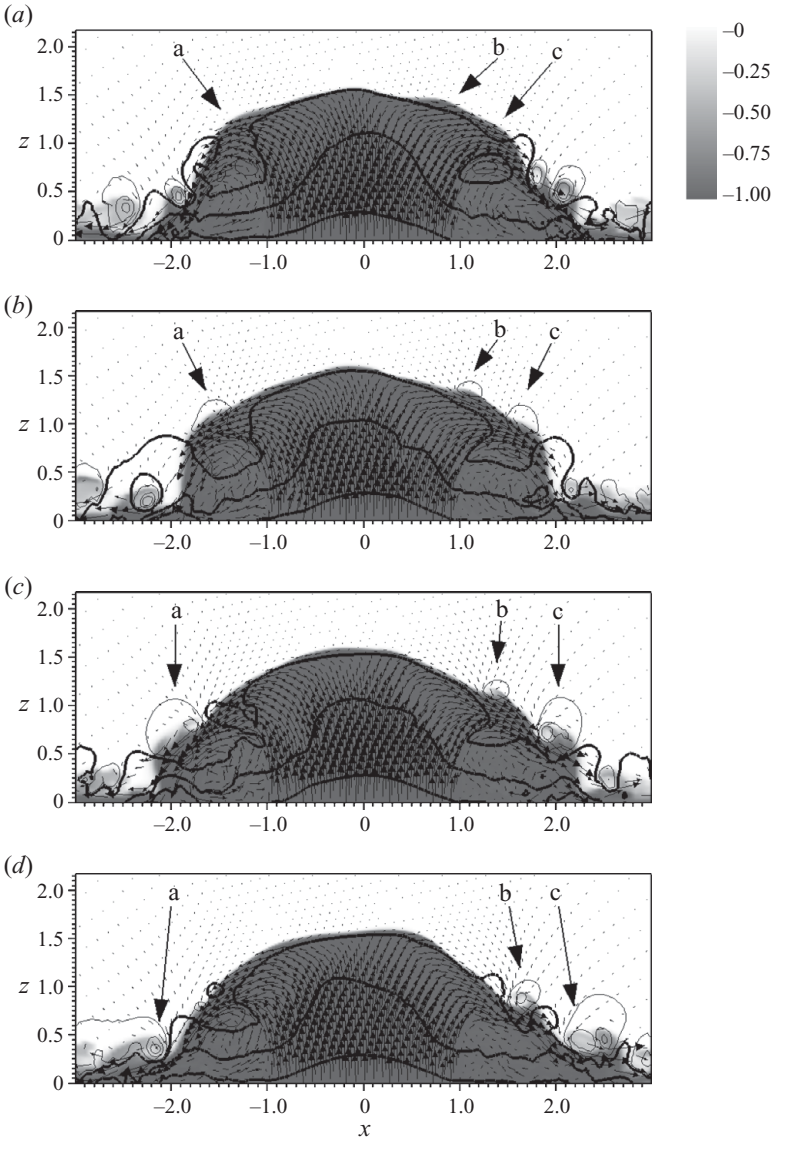

FIGURE 4. Flow structure of $Fr = 0.97$, $Re = 3494$, $Pr = 0.7$ simulation at $t = 16$, 16.75, 17.5 and 18.25, respectively. Shading indicates ϕ (scale on right) and vectors are scaled to give velocity magnitude. Thick lines give p contours of 0.05, 0.3 and 0.7, thin lines give contours of −0.5, −0.25 and −0.05.

of ambient fluid into the fountain core. K–H vortices form in the cap region and flow into the intrusion. They appear to be initiated by the deformation of the cap region and then driven by shear and baroclinic torque in the outflow. The same behaviour is seen at $Fr = 0.97$ and $Fr = 1.4$ as illustrated in figures 4 and 5. In figure 4 the development of three K–H structures is followed from an initial perturbation in figure 4(a) through its growth in figure 4(b,c) and flow into the intrusion in figure 4(d). One notable difference between the $Fr = 0.4$–1.4 simulations and the $Fr = 0.1$ simulation is the presence of a small re-circulation region surrounding the source. Ambient fluid

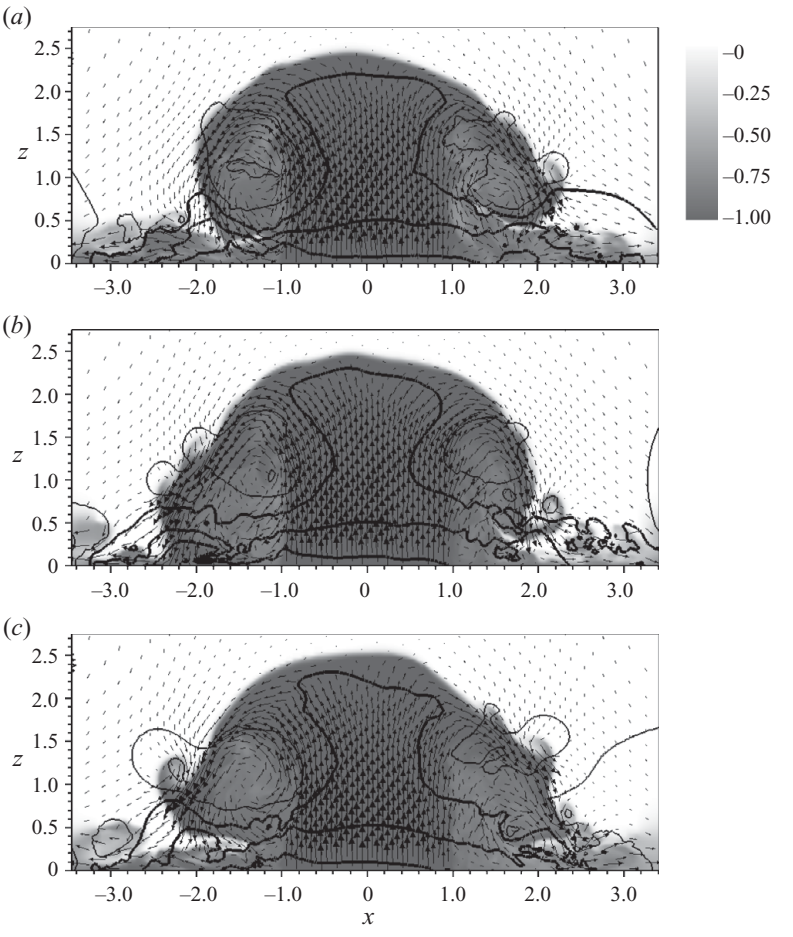

FIGURE 5. Flow structure at $Fr = 1.4$, $Re = 3494$, $Pr = 0.7$ from $t = 13.2$ in increments of $\Delta t = 3.3$. Shading indicates ϕ (scale on right) and vectors are scaled to give velocity magnitude. Thick lines give p contours at 0.1, 0.3 and 0.5 and thin lines contours at -0.33 and -0.05.

initially in this region is quickly advected out into the intrusion. At $Fr = 0.97$, the size of the annular re-circulation region adjacent to the upflow is illustrated by the velocity vectors in figure 4. The mixing eventually depletes the ambient fluid in this region and no additional ambient fluid is entrained. This mixing behaviour is illustrated in supplementary movies 1, 2 and 3 (available at journals.cambridge.org/flm).

At $Fr = 1.4$ the re-circulation region covers more than half the overall fountain height. The fountain fluid rises in a coherent column before stagnating in the cap region where it is forced radially outwards in large periodic expulsions, which are not necessarily symmetric around the source axis. The distinction from the $Fr = 0.97$ flow is that there is mixing of ambient fluid into the annular re-circulation region as shown in figure 5(*a–c*). From figure 5(*a*) ambient fluid is drawn into the adjacent re-circulation zone, then in figure 5(*b*) there is a large expulsion from the cap region. In figure 5(*c*) the fountain rises again drawing in ambient fluid before the next downflow. In this way the oscillation in fountain height, the accumulation and expulsion of fluid from the cap region and the entrainment of ambient fluid operate on the same cycle

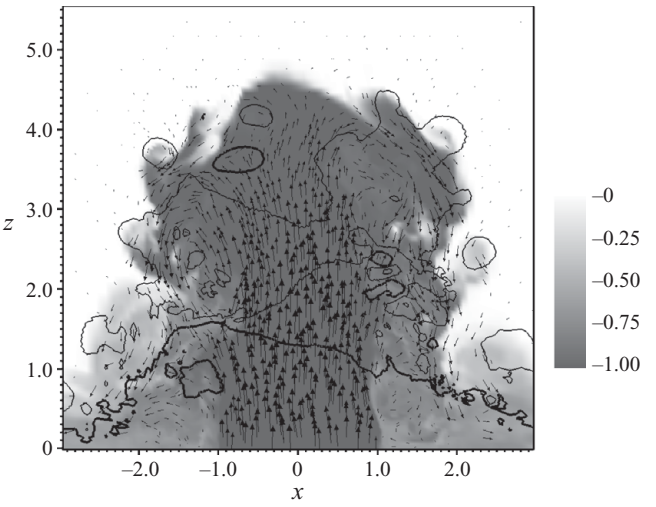

FIGURE 6. Flow structure of $Fr = 2.1$, $Re = 3494$, $Pr = 7.0$ flow at $t = 35$. Shading indicates ϕ (scale on right) and vectors are scaled to give relative velocity magnitude. Thick lines indicate p contours of 0.03 and 0.25; thin lines give p contours of -0.25 and -0.03.

which has approximately the same period as one overturn of the re-circulation region, $t \sim 6$–7 for $Fr = 1.4$. The time trace of this behaviour is illustrated in § 4.

At $Fr = 2.1$, the flow is no longer characterized by a permanent re-circulation region but by an extended mixing regime with clearly defined boundaries between the upflow, downflow and ambient fluid (see figure 6). The inner upflow stream is short however and the annular shear layer does not merge. The cap region of the flow is similar to the $Fr = 1.4$ flow, with periodic non-axisymmetric ejection of fluid from the cap region. The ejection of dense fluid at one side of the fountain increases the strength of the local downflow and drives large-scale structures that increase mixing, as illustrated in Williamson *et al.* (2008*a*). This behaviour also sets the period of oscillation in the fountain height. The outflowing fluid forms an annular vortex around the cap region in a similar way to the $Fr = 1.4$ flow re-circulation region. In figure 6 the pressure contours and shading of ϕ illustrate the K–H structures at the top interface and the strong annular vortex at the head of the fountain. The intrusion forms at the base of the fountain causing a local high-pressure region there.

4. Initial transient flow behaviour

The centreline height of the fountain rises to its maximum and then oscillates about a lower mean value after which flow statistics are obtained. The time trace of the source pressure and the maximum penetration height, defined as the point where $\phi = 0.5$, are given in figure 7. Lin & Armfield (2003) showed that in steady-low-Froude-number fountain flow, $\phi = 0.5$ coincides with $u_z = 0$ and is therefore a reasonable measure of fountain height in unsteady conditions. The starting rise times vary according to different time scales.

The initial rise time of high-Froude-number turbulent fountains was shown to scale on $t_m \sim Fr^2$ empirically by Pantzlaff & Lueptow (1999) and then by Williamson *et al.* (2008*b*) for laminar high-Froude-number fountain flow. The time scale for the weak flow regime may be obtained using the zero entrainment model proposed by Zhang & Baddour (1997) and Kaye & Hunt (2006). They assumed direct conversion of kinetic

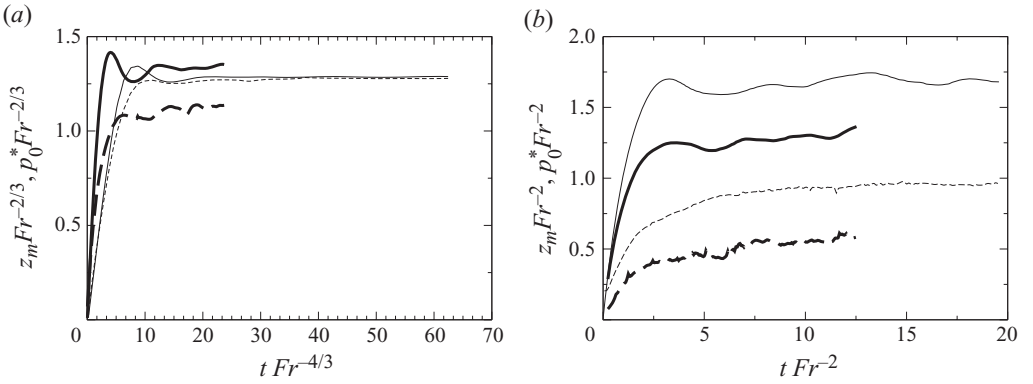

FIGURE 7. Time evolution of fountain height and normalized source pressure head $p_0^* = p_0 Fr^2$, at $r = 0$ and $z = 0$. Dashed lines indicate $p_0^*(t)$ and solid lines indicate $z_m(t)$. (*a*) $Fr = 0.1$ is indicated by thin lines and $Fr = 0.4$ by thick lines. (*b*) $Fr = 0.97$ is indicated by thin lines and $Fr = 1.4$ by thick lines. In both cases $Re = 3494$ and $Pr = 0.7$. Scaling as indicated on axis.

energy to potential energy so $U_0^2 = 2\sigma_0 Z_m$ giving $z_m \sim Fr^2$. We use the same arguments for the time scaling, where dimensional time $T_m = U_0/\sigma_0$ giving $t_m \sim Fr^2$, the same as for the high-Froude-number flow regime. Lin & Armfield (2000*a*) found that the rise time of fountain flow over the range $0.1 \leqslant Fr \leqslant 1.0$ followed a $t_m \sim Fr^2$ scaling. For very weak fountains they obtained $t_m \sim Fr^{4/3}$ based on dimensional grounds and confirmed the relation with numerical simulations over the range $0.05 \leqslant Fr \leqslant 0.2$ (Lin & Armfield 2000*b*). This suggests a two-regime scaling for fountain rise time, a forced–weak regime where $t_m \sim Fr^2$ and the very weak regime where $t_m \sim Fr^{4/3}$.

The source pressure is shown to be important in §§ 5 and 6, so is plotted here together with the penetration height. In figure 7(*a*) the time trace of fountain penetration height and source pressure at $Fr = 0.1$ and $Fr = 0.4$ are scaled with $t_m \sim Fr^{4/3}$ and $z_m \sim Fr^{2/3}$ while in figure 7(*b*) the results at $Fr = 0.97$ and $Fr = 1.4$ are scaled by $t_m \sim Fr^2$ and $z_m \sim Fr^2$. Across this Froude number range the flow regime changes so the flow quantities are not expected to scale well and this is borne out in the results. The rise time at $Fr = 0.1$ and $Fr = 0.4$ are not collapsed by $t_m \sim Fr^{4/3}$ while the penetration height performs well but with the contribution of the pressure head reduced at $Fr = 0.4$. At $Fr = 0.97$ and $Fr = 1.4$ the $t_m \sim Fr^2$ scaling collapses the time scale for both results well but Z_m does not collapse with the $z_m \sim Fr^2$ scaling, derived using the same arguments. However, if the source pressure component is subtracted from the total height the difference, $z_m - p_0 Fr^2$ scales with approximately Fr^2.

In figure 8, the fountain mean penetration height, defined as the point where the mean vertical velocity $\bar{u}_z = 0$, is plotted against Froude number together with the other published results for this range of Froude numbers. There is a high degree of correspondence between the high-Reynolds-number simulations in this study and the previous results across the entire range of values simulated. The very weak points at $Fr = 0.1$ and $Fr = 0.4$ coincide with Lin & Armfield (2000*a*,*b*) $Re = 200$ results and their relation $z_m = 1.26 Fr^{2/3}$ (Lin & Armfield 2000*b*), not withstanding the difference in Reynolds numbers between these previous studies. Lin & Armfield (2000*a*) found that their numerical results for $Fr = 0.2$–1.0 were best fitted by a $z_m \sim Fr$ scaling, but from figure 8 it is clear that this region is part of a transition range between the weak $z_m \sim Fr^2$ regime and very weak flow $z_m \sim Fr^{2/3}$. We examine the behaviour of the very weak regime in § 5 and the transition to the weak regime in § 6.

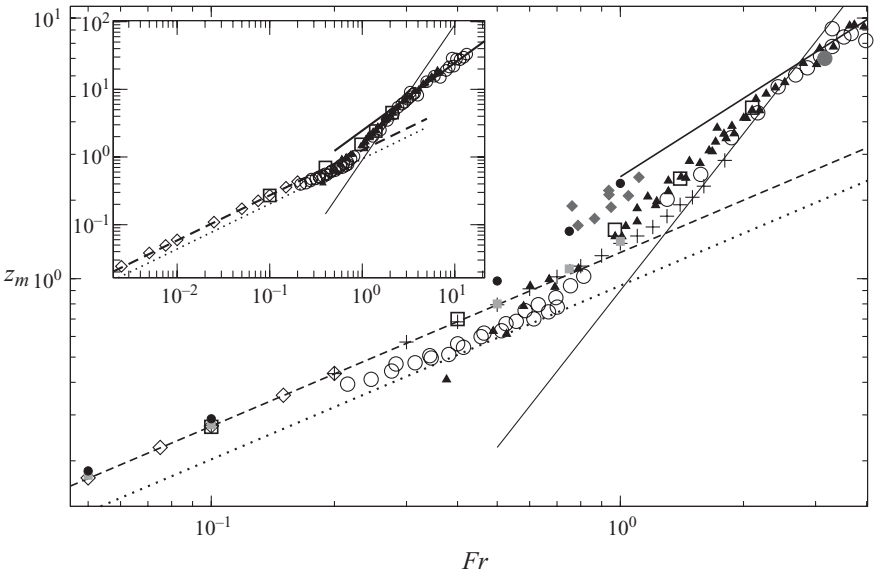

FIGURE 8. Normalized fountain penetration height with Froude number where the dashed line is $1.26Fr^{2/3}$ (Lin & Armfield 2000*b*), the dotted line $0.94Fr^{2/3}$ (Kaye & Hunt 2006), the thin solid line $0.9Fr^2$ (Kaye & Hunt 2006) and the thick solid line $2.46Fr$ (Turner 1966). Symbols: ○, Kaye & Hunt (2006); ◇, Lin & Armfield (2000*b*); +, Lin & Armfield (2000*a*) (uniform source velocity profile); ▲, Zhang & Baddour (1998); ●, Cresswell & Szczepura (1993); ◆, Williamson *et al.* (2008*b*); □, the present simulations at $Re = 3494$ with an unsteady inlet condition; ■ and • indicate $Re = 250$ with uniform and parabolic inlet source velocity profiles, respectively.

5. Very weak flow

The results have been interpolated onto a cylindrical coordinate system (r, z, θ) and statistics calculated. The terms in the axial momentum equation are plotted against fountain axial location from the centre of the source to the maximum penetration height at $r = 0$ in figure 9. At $Fr = 0.1$ (figure 9*a*) advection is negligible and the flow is primarily a balance between axial pressure gradient and buoyancy. The result supports the suggestion of Zhang & Baddour (1998) that the relevant length scale for the flow is $Z_m = f(Q_0, F_0)$ and is not a function of M_0.

Very weak flow behaviour is governed by the radial momentum balance and is directly affected by the intrusion. The effect of viscosity on the very weak flow regime has been tested with two simulations with uniform inlet velocity profile at the source for $Fr = 0.1$ at $Re = 250$, $Pr = 4$ and $Re = 20$, $Pr = 50$. The Prandtl number has been varied to ensure diffusive scalar transport, which goes like $1/RePr$, and is similar in the low Reynolds number regime (Lin & Armfield 2003).

The radial momentum balance terms for $Fr = 0.1$ are given in figure 10(*a–c*) together with two definitions of the fountain/intrusion depth. The line of $\phi = 0.1$, indicated by z_ϕ, is observed to coincide approximately with the top of the upper mixing layer/ambient interface. $\bar{z}$, the local depth averaged intrusion height defined as

$$\bar{z}(r) = \int_0^{z_m} \left(\frac{1}{2\pi} \int_0^{2\pi} \phi(r, z, \theta)\, \mathrm{d}\theta \right) \mathrm{d}z, \tag{5.1}$$

is observed to lie between the dense intrusion and the upper mixing layer.

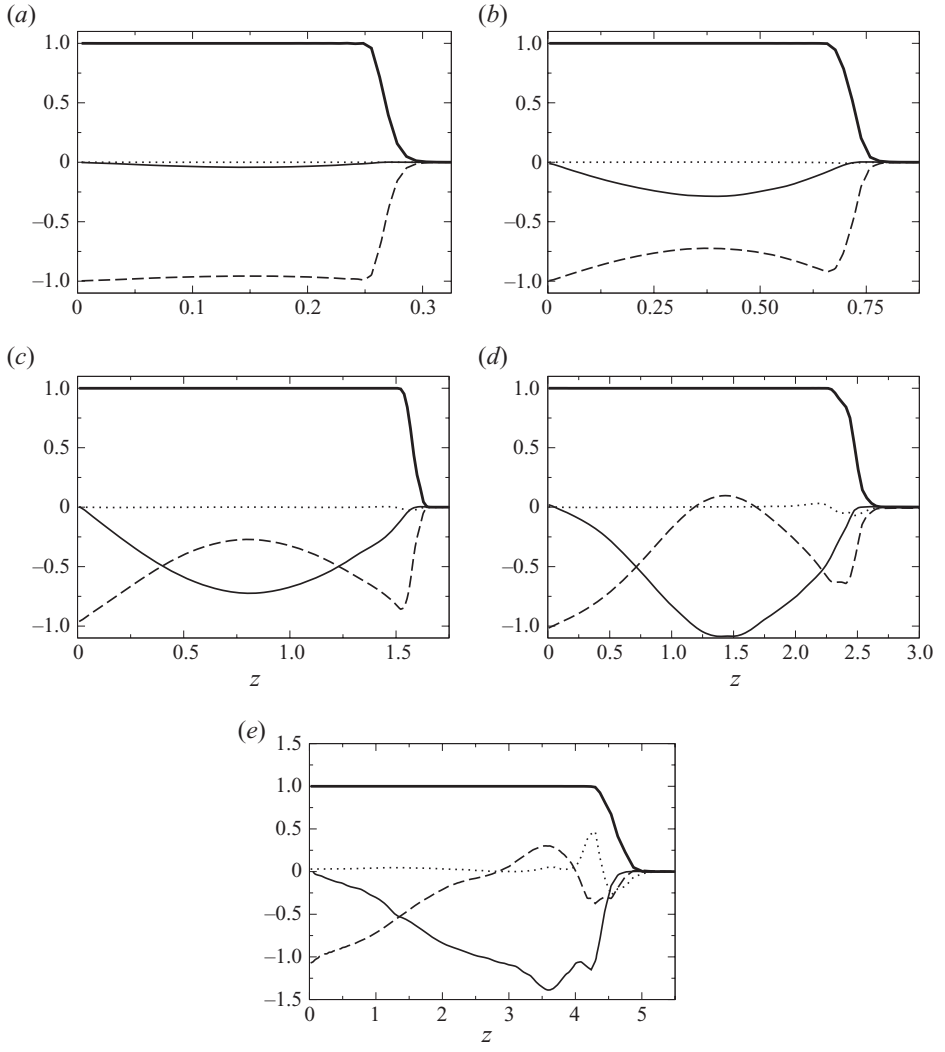

FIGURE 9. Vertical momentum balance of $Re = 3494$ simulations at $r = 0$ for (a) $Fr = 0.1$, $Pr = 0.7$, (b) $Fr = 0.4$, $Pr = 0.7$, (c) $Fr = 0.97$, $Pr = 0.7$, (d) $Fr = 1.4$, $Pr = 0.7$ and (e) $Fr = 2.1$, $Pr = 7.0$. Thick line, buoyancy $[\bar{\phi}]$; thin line, advection $[(\bar{u}_r\,\partial\bar{u}_z/\partial r + \bar{u}_z\,\partial\bar{u}_z/\partial z)Fr^2]$; dashed line, pressure gradient $[\partial\bar{p}/\partial z\,Fr^2]$; dotted line, turbulent diffusion $[(1/r\,\partial r\overline{u_z'u_r'}/\partial r + \partial\overline{u_z'u_z'}/\partial z)Fr^2]$. Viscous diffusion $[-1/Re(1/r\,\partial(r\partial\bar{u}_z/\partial r)/\partial r + \partial^2\bar{u}_z/\partial z^2)Fr^2]$ is negligible and not shown. All variables are in non-dimensional form.

All the simulations are unsteady, however, the nature of the unsteadiness is different for the turbulent and laminar simulations. The high-Reynolds-number case reaches a quasi-steady flow regime after $t = 1.4$, where the intrusion behaviour is statistically steady. The statistics presented in figure 10(c) are obtained by time averaging over $t = 1.4$–2.8, enough for 20 K–H structures to move through the intrusion. The two-low-Reynolds-number simulations do not reach this quasi-steady state and the intrusion continues to grow with time. The results in figure 10(a,b) are instead azimuthally averaged at one instant of time and the transient term, which does not go to zero, is also presented.

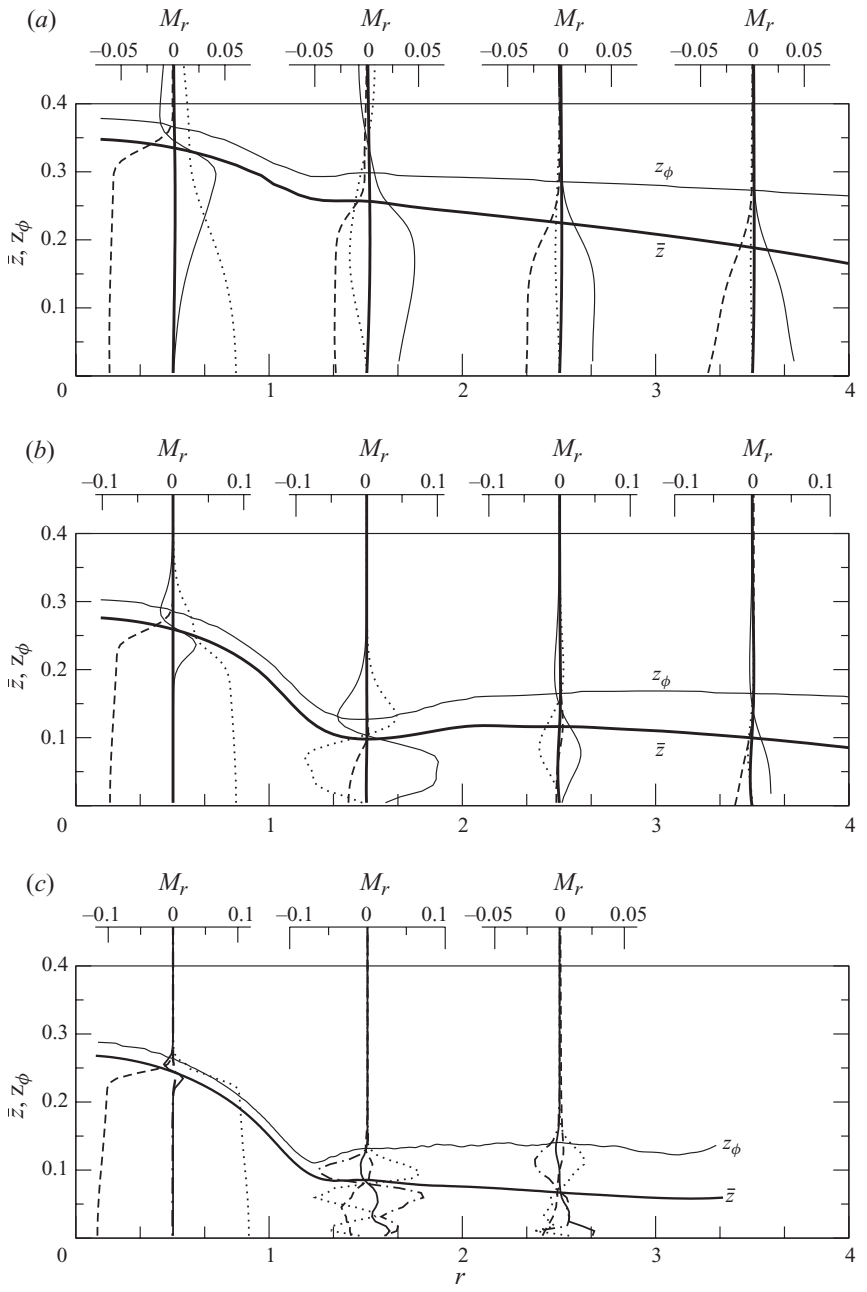

FIGURE 10. Radial momentum balance given at locations from the fountain source through the intrusion where radial location is indicated by the lower abscissa and local momentum balance indicated by upper abscissa labelled M_r. Results given for $Fr = 0.1$ at (*a*) $Re = 20$ and $Pr = 50$ at $t = 2.5$, (*b*) $Re = 250$ and $Pr = 4$ at $t = 2.5$ and (*c*) $Re = 3494$ and $Pr = 0.7$ with statistics averaged over $t = 1.4$–2.5. The momentum balance terms are indicated by thick dotted line, $[(\bar{u}_r\,\partial\bar{u}_r/\partial r + \bar{u}_z\,\partial\bar{u}_r/\partial z)Fr^2]$; thin solid line, $[-1/Re(1/r\,\partial(r\,\partial\bar{u}_r/\partial r)/\partial r + \partial^2\bar{u}_r/\partial z^2 - \bar{u}_r/r^2)Fr^2]$; thick dashed line, $[\partial\bar{p}/\partial r\,Fr^2]$; thick solid line, $[d\bar{u}_r/dt\,Fr^2]$; thick dashed–dotted line, $[(1/r\,\partial r\overline{u_r'u_r'}/\partial r + \partial\overline{u_r'u_z'}/\partial z - \overline{u_\theta'u_\theta'}/r)Fr^2]$. All terms are non-dimensional. Overlaid is a plot of fountain/intrusion height defined firstly ($\bar{z}$) by (5.1) (thick solid line) and secondly (z_ϕ) by the location of $\phi = 0.1$ (thin solid line).

In the cap region the momentum balance is dominated by the radial pressure gradient and the radial advection term with viscous effects only important at the interface and only at low Reynolds number. In all three cases the start of the intrusion occurs at $r \approx 1.5$. From this point onwards the flow behaviour depends strongly on the Reynolds number.

At $Re = 20$, the flow decelerates into the intrusion against viscosity and the pressure gradient continues to drive the flow. By $r = 2.5$, the flow is predominantly a balance between viscosity and pressure gradient. The head required to drive the flow against viscosity continues to increase with penetration of the intrusion so the fountain height continues to increase. In this way, at $Re = 20$, the fountain dynamic is one where the height is directly linked to the depth and extent of the intrusion.

At $Re = 250$, r between 1.5 and 2.5 viscous effects decelerate the flow with the radial pressure gradient less significant than at $Re = 20$. The depth of the intrusion also increases over this region, coinciding with the subcritical Froude number as shown in the figure. At $r = 3.5$ the flow again returns to a balance between viscosity and pressure gradient and behaves as the $Re = 20$ flow. In the subcritical region the flow depth increases with time and will presumably eventually overwhelm the fountain. The clearly defined diffusive mixing layer above the intrusion is accelerated by viscous forces.

At $Re = 3494$ the flow is more complex owing to the turbulent mixing in the intrusion. At $r = 1.5$ momentum is dissipated by viscosity, via $(1/Re\, d^2\bar{u}_r/dz^2)$ and transported by turbulent diffusion to the upper layer through $d\overline{u_r' u_z'}/dz$. The formation of the lower boundary layer and the upper mixing layer where the flow leaves the fountain and enters the intrusion creates the double peaked deceleration profile. The lower peak is a balance between viscosity at the lower wall and turbulent diffusion, and the upper peak is predominantly a result of mixing between the intrusion and the upper mixing layer. The radial pressure gradient is significant. In the upper mixing layer ambient fluid is entrained and accelerated into the intrusion primarily by turbulent diffusion. At $r = 2.5$ the upper mixing layer is unchanged but in the intrusion the pressure gradient is reduced. The flow passes out through the outlet boundary condition with no observable effect on the simulation.

Also important to the discussion is the local depth averaged Froude number for the radial flow in the intrusion, $Fr_r(r)$. This is illustrated in figure 11 together with $\bar{z}(r)$, for $Fr = 0.97$, 0.4 and 0.1 at $Re = 3494$ and additionally for the viscous flow simulations at $Fr = 0.1$ at $Re = 20$ and $Re = 250$. The non-dimensional quantities are defined as

$$Fr_r(r) = \frac{\bar{u}_r(r) Fr}{\sqrt{\bar{z}(r)}} \tag{5.2}$$

where $\bar{u}_r$ is given by

$$\bar{u}_r(r) = \frac{\displaystyle\int_0^{z_m} \left(1/2\pi \int_0^{2\pi} u(r, z, \theta)\phi(r, z, \theta)\, \mathrm{d}\theta \right) \mathrm{d}z}{\displaystyle\int_0^{z_m} \left(1/2\pi \int_0^{2\pi} \phi(r, z, \theta)\, \mathrm{d}\theta \right) \mathrm{d}z}, \tag{5.3}$$

respectively. Figure 11 illustrates the development of the intrusion through the quasi-steady flow. For $Fr = 0.1$–0.97 at $Re = 3494$, the intrusion flow is supercritical through the extent of the domain simulated. The initial rise and establishment of the flow causes the intrusion front to form with the local Fr_r being supercritical but subcritical immediately behind the fountain region. After this passes the intrusion extends into

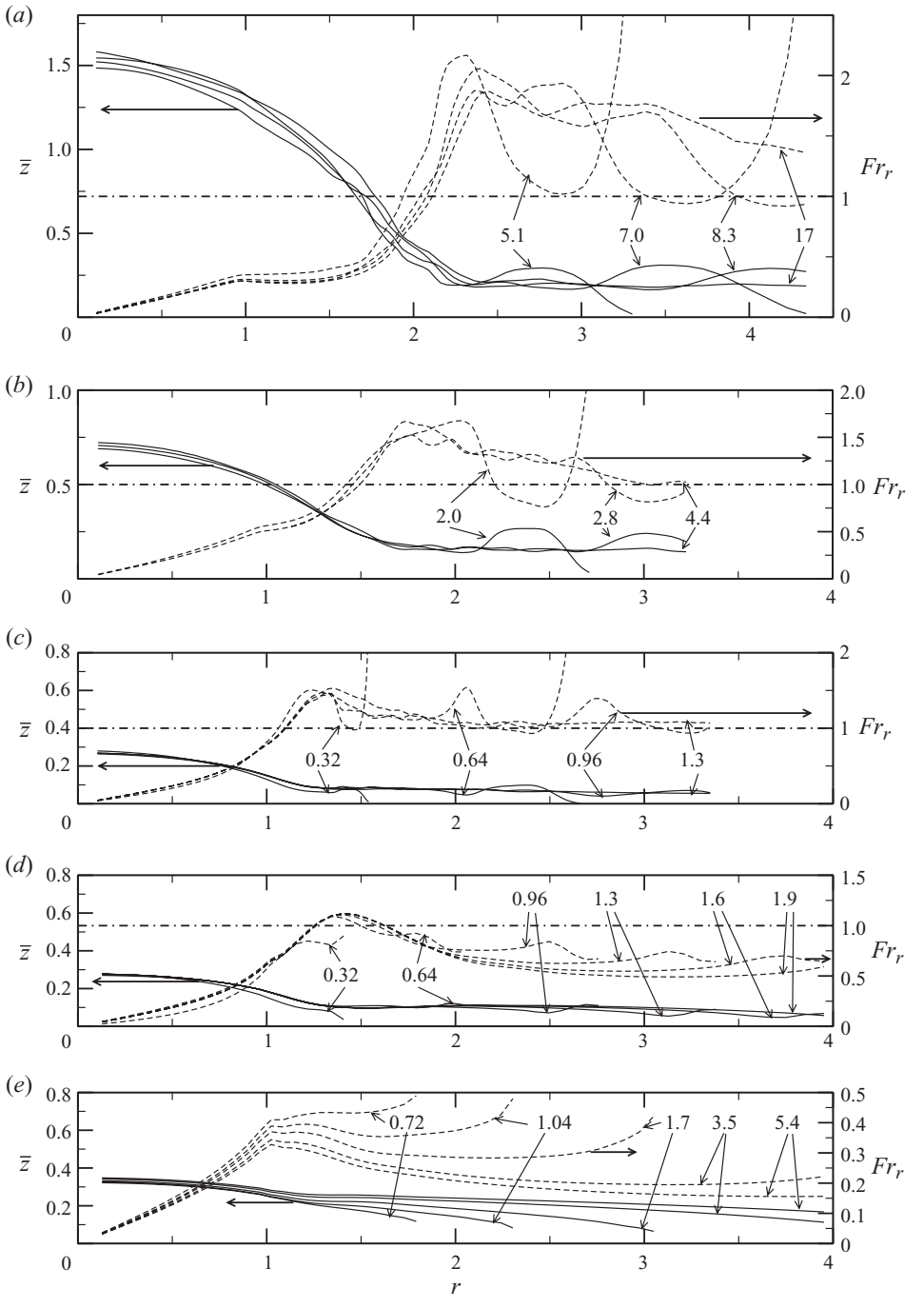

FIGURE 11. Fountain intrusion behaviour for (*a*) $Fr = 0.97$, (*b*) $Fr = 0.4$ and (*c*) $Fr = 0.1$ at $Re = 3494$, $Pr = 0.7$ with indicated non-dimensional time. Uniform source velocity profile runs at $Fr = 0.1$ with $Re = 250$, $Pr = 4$ (*d*) and $Re = 20$, $Pr = 50$ (*e*). Solid line, $\bar{z}$; dashed line, Fr_r; dash–dotted line, $Fr_r = 1.0$.

the domain with constant input of mass flux. The increased viscous dissipation in the low-Reynolds-number simulations and the increased depth have the effect of forcing the flow back to a subcritical Fr_r away from the intrusion origin. At $Re = 250$ the local Fr_r maximum occurs at $r \approx 1.4$ and is subcritical for $r \gtrsim 1.6$. At $Re = 20$ the flow is subcritical everywhere and the intrusion is more directly connected with the source. An additional simulation, not shown here for brevity, was performed at $Re = 100$ and found to be fully subcritical also, so the transition between fully subcritical flow and flow that is critical near the intrusion source occurs in the range $Re = 100$–250.

The scaling for the fountain height can be interpreted from the results as follows: For $Re \gtrsim 250$ the intrusion flow around the source is supercritical and viscous effects at the source are small. The radial pressure gradient drives radial acceleration such that $1/\rho_0 \, \mathrm{d}P/\mathrm{d}R = \mathrm{d}U_r U_r/2\mathrm{d}R$. The pressure head at the centre of the source ($Z = 0$, $R = 0$) is $P_0 = Z_m \Delta\rho g$. Where the fountain meets the intrusion at $R = R_e$, $P_e \approx 0$. The fountain fluid accelerates from $U_r = 0$ to $U_e = Q_0/A_e$ from $R = 0$ to $R = R_e$. In very weak flow where there is no re-circulation region, $R_e = R_0$ (or $r_e = 1$). Following Kaye & Hunt (2006) by using the analogy of critical flow weir flow, the fountain height at $R = R_e$ will be $H_e = 2Z_m/3$. This gives $U_e = Q_0/A_e = Q_0/2\pi R_e H_e = 3U_0 \pi R_0^2/2Z_m 2\pi R_e$. In this way $1/\rho_0 \, (P_0 - P_e)/R_e \approx (U_e)^2/2R_e$ so $z_m \approx 0.66 Fr^{2/3} C_r^{2/3}$, where $C_r = R_0/R_e$, confirming the scaling found by Lin & Armfield (2000*b*) $z_m = 1.26 Fr^{2/3}$, and Kaye & Hunt (2006) $z_m = 0.94 Fr^{2/3}$, although with variation in the coefficients.

Figure 10 shows that the pressure gradient does not tend to zero at $r = 1$ but continues into the intrusion and is significant until $r \gtrsim 1.5$. The full balance for the pressure gradient at the source must then include the additional backpressure around the source. In this way where the pressure gradient remaining at the edge of the source is given by $(\mathrm{d}\bar{p}/\mathrm{d}r)_e = (\mathrm{d}\overline{u_r' u_z'}/\mathrm{d}z + 1/Re \, \mathrm{d}^2\bar{u}_r/\mathrm{d}z^2 - \mathrm{d}\bar{u}_r\bar{u}_r/2\mathrm{d}r)_e$. The term $(\mathrm{d}\bar{p}/\mathrm{d}r)_e$ is a function of Reynolds number and Froude number so would suggest a relation of the form $z_m = f(Fr) + f(Re, Fr)$ where the first term on the right-hand side is the acceleration term described above and the second term is the additional effect of the intrusion.

From $Re = 250$ to 3350, the radial pressure gradient around the source at $r = 1.5$ is comparable in magnitude although the behaviour varies from laminar viscous flow to a turbulent boundary layer flow. This has the result that z_m is only slightly affected by the Reynolds number. It is clear in figure 8 that the z_m measurements at $Re = 3494$ and $Re = 250$ both lie on $z_m = 1.26 Fr^{2/3}$ for $Fr < 0.4$ so the Reynolds number effect is small, constant and has the same Froude number scaling. This is not surprising as the flow geometry also can be shown to scale with $\sim Fr^{2/3}$. Because $Fr_r = 1$, $h_e = 2z_m/3$ and $z_m \sim Fr^{2/3}$, the scaling for the intrusion depth at the source is $h_e \sim Fr^{2/3}$. The results can then be summarized as $z_m = (A_1 + A_2) Fr^{2/3}$, where A_1 and A_2 are constants representing the separate effects of radial acceleration at the source and the backpressure from the intrusion, respectively.

In figure 8, the fountain penetration height measurements of Zhang & Baddour (1998) and Kaye & Hunt (2006) are clearly much smaller than those in the present study or in Lin & Armfield (2000*b*). The key difference between these studies is the nozzle configuration. Zhang & Baddour (1998) and Kaye & Hunt (2006) appear to use a re-entrant nozzle configuration whereas the others are flush mounted with the lower wall and are therefore affected by the intrusion.

For $Re \lesssim 100$ the flow is subcritical, viscous and governed by the extent of the intrusion in a viscous hydraulic balance, a quite different flow which has been addressed by Huppert (1982) and Snyder & Tait (1995). The present work then suggests two regimes of flow behaviour with the transition in the range $Re = 100$–250.

6. Very weak to weak flow

In the axial momentum balance in figure 9, the transition from very weak flow at $Fr = 0.1$ to weak flow at $Fr = 2.1$ can be seen quantitatively as an increase in the advection term at the expense of the pressure gradient. The fluid enters the domain with zero mean radial velocity so the axial acceleration term is zero and the buoyancy force is balanced by an axial pressure gradient. As the flow rises, it decelerates and the axial pressure gradient decreases. Continuity requires that the fluid accelerate radially. The axial advection term rises to its maximum value and then decreases to zero where the fluid approaches the stagnation point and the flow reverts to a balance between axial pressure gradient and gravity. Turbulent diffusion is negligible through the fountain core, only becoming significant at the oscillating top interface with the ambient fluid for $Fr = 1.4$ and $Fr = 2.1$.

A vector plot of the mean flow at $Fr = 1.4$ in figure 12(a) shows how the flow rises and flows outwards above the re-circulation zone. In figure 12(b–f) contour plots of the balance terms in the radial and axial momentum equations are presented. The radial acceleration peaks above the re-circulation region at the outflow ($r \approx 1$, $z \approx 1.4$), while the axial acceleration peaks just before the cap region.

In the absence of viscous or turbulent diffusion the total pressure $p_T Fr^2 = z_m + p_t Fr^2 = p_0 Fr^2 + 1/2(u_z Fr)^2$, where p_t is the non-dimensional static pressure remaining at the top of the fountain stagnation point. The source velocity head is a constant so the behaviour of p_0 is examined here.

If the flow can be decomposed into two regions as $z_m = h_c + h_r$ where h_c is the non-dimensional cap region height and h_r is the height of the re-circulation zone/upflow column illustrated in figure 13(b), the two regions may be modelled separately. Using the very weak flow model, the cap region may be assumed to be hydraulically controlled so

$$h_c \approx (p_0 - p_t) Fr^2, \tag{6.1}$$

and $h_c = C_1 (Fr C_r)^{2/3}$. This leaves

$$h_r \approx \tfrac{1}{2}(uFr)^2, \tag{6.2}$$

or $h_r = C_2 Fr^2$, which is the zero entrainment scaling. In table 2, h_r is defined arbitrarily as the maximum axial location reached by a Lagrangian particle trajectory, in the mean flow field, originating from the fountain source at $r = 0.99$. This point also coincides with the axial location of maximum radial acceleration illustrated in figure 12(e). In the same table the other terms in the hydraulic energy balance between $z = 0$ and $z = z_m$ at $r = 0$ are given. For the laminar results (6.1) and (6.2) are shown to hold. The hydraulic balance is not as close for the turbulent simulations results but this could be an effect of the inlet velocity profile.

The correlation coefficients C_1 and C_2 are given in the table for both the fully turbulent simulation results together with uniform inlet velocity laminar simulation results from $Fr = 0.05$ to 1.0. For the cap region/very weak flow, C_1 decreases from 1.3 to 1.1 in both laminar and turbulent simulations as the influence of the intrusion is reduced but not to the 0.66 limit suggested in § 5.

Using the source centreline velocity in (6.2) of $u_z = 1.0$ for the uniform simulations and $u_z = 1.31 U_B / U_0$ for the turbulent simulations, the expected values of C_2 are 0.5 and 0.79, respectively. The measured values of C_2 given in the table are 0.57–0.5 for the uniform runs and 0.56–0.7 for the non-uniform turbulent profiles.

The radial location of h_r, r_e and the depth of the outflow at this location, h_e, are given in the table together with $2h_c/3$, the depth predicted for critical weir flow and

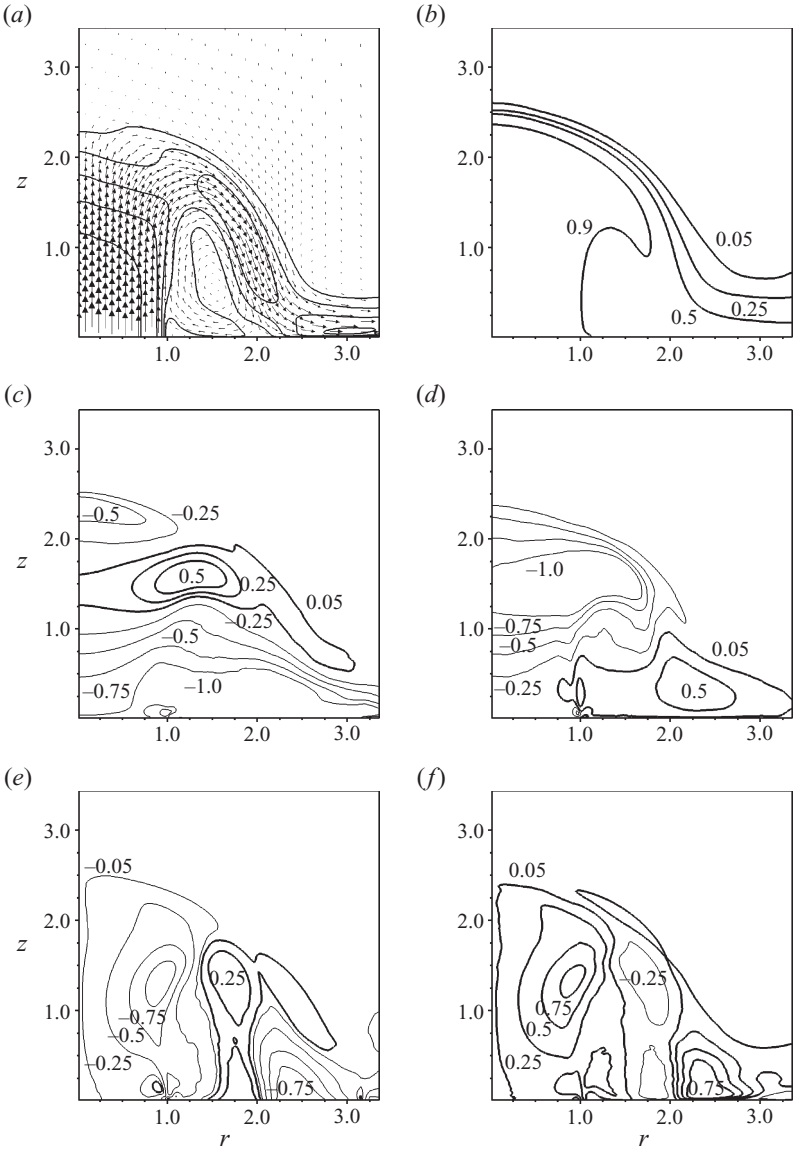

FIGURE 12. $Fr = 1.4$, $Re = 3494$, $Pr = 0.7$ result with (a) mean velocity vectors and velocity magnitude contours; (b)–(d) contours of axial momentum balance terms $[\bar{\phi}]$, $[\partial \bar{p}/\partial z\, Fr^2]$ and $[(\bar{u}_r\, \partial \bar{u}_z/\partial r + \bar{u}_z\, \partial \bar{u}_z/\partial z)Fr^2]$, respectively; ($e$) and ($f$) contours of radial momentum balance terms $[\partial \bar{p}/\partial r\, Fr^2]$ and $[(\bar{u}_r\, \partial \bar{u}_r/\partial r + \bar{u}_z\, \partial \bar{u}_r/\partial z)Fr^2]$, respectively.

assumed in the scaling model. The comparison is generally very good, supporting the model assumptions. The variation in behaviour between turbulent and laminar results suggests the inlet profile may have an affect on this.

The flow in the cap region at $Fr = 2.1$ is more dynamic and the flow is structurally different with an extended mixing region, so the approach described to separate the two regions is not possible. In table 2 the height of the cap region is inferred using the assumption that $h_c \approx p_0 Fr^2$ for comparison. There is increased energy loss from

Fr	z_m	$(p_0 - p_t)Fr^2$	$1/2\,(uFr)^2$	h_r	h_c	r_e	h_e	$2h_c/3$	C_1	C_2
0.05	0.18	0.18	0.001	0	0.18	1	0.17	0.12	1.3	
0.1	0.28	0.27	0.005	0	0.28	1	0.18	0.18	1.3	
0.5	0.8	0.67	0.13	0.14	0.66	1.2	0.41	0.44	1.2	0.57
0.75	1.09	0.82	0.28	0.3	0.79	1.31	0.51	0.53	1.1	0.53
1	1.39	0.90	0.50	0.5	0.89	1.35	0.57	0.59	1.1	0.5
0.1	0.27	0.26	0.01	0.00	0.27	1.00	0.15	0.18	1.3	
0.40	0.72	0.58	0.13	0.09	0.63	1.13	0.36	0.42	1.3	0.56
0.97	1.58	0.82	0.74	0.60	0.98	1.20	0.64	0.65	1.1	0.64
1.4	2.54	1.01	1.54	1.37	1.17	1.33	0.67	0.78	1.1	0.70
2.1	4.53	1.38	3.43	3.43*	1.38*	1.0*	0.82	0.92	0.84	0.78

TABLE 2. Hydraulic energy balance at $r = 0$ and interpreted scaling results for very weak to weak fountains at $Re = 250$ with uniform source velocity profile (upper set) and $Re = 3494$ with non-uniform/turbulent inlet profile (lower set). Coefficients are $C_1 = h_c(1/FrC_r)^{2/3}$ and $C_2 = h_r/Fr^2$. *: not measured, calculated for comparison assuming $h_c = p_0Fr^2$.

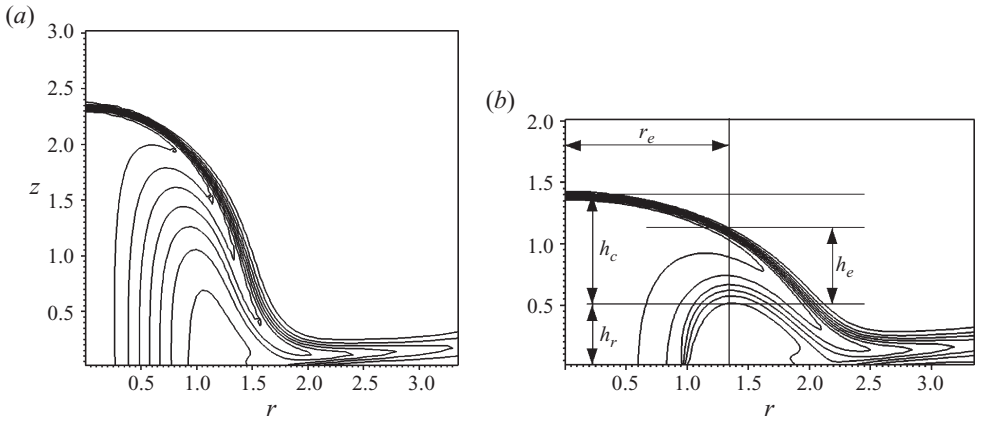

FIGURE 13. Contours of total pressure $[p_T = (1/2)u^2 + z\phi/Fr^2 + p]$ for (a) parabolic and (b) uniform source velocity inlet profile at $Re = 250$ and $Fr = 1.0$.

turbulent diffusion so the penetration height is less than the source pressure and centreline momentum flux.

Additional runs were performed at $Re = 250$ and $Fr = 0.05, 0.1, 0.5, 0.75, 1.0$ for both parabolic and uniform source velocity profiles. The results presented in figure 8 show that the uniform and parabolic results have nearly the same penetration height for $Fr = 0.05$–0.1 but above $Fr = 0.5$ the parabolic profile penetrates a greater distance. The low-Reynolds-number steady fountain simulations from Williamson *et al.* (2008*b*) are included in this figure with the Froude numbers calculated assuming fully parabolic velocity profiles. The Reynolds numbers are small ranging within $Re = 56$–92. Lin & Armfield (2003) suggested that at these Reynolds and Froude numbers, the height is increased approximately 10–12 % by viscous effects ($z_m = 1.324 + 1.346/Re^{1/2}$ for $Fr = 1$; Lin & Armfield 2003, (35)). The measurements compare well with the parabolic numerical results.

The difference between the penetration heights of the two profiles as a result of higher centreline velocity is not captured locally in the definition of the Froude

number, which is a bulk value. The plot of total pressure ($p_T = 1/2\ u_i^2 + z\phi/Fr^2 + p$) for parabolic and uniform source velocity profiles at $Fr = 1$ and $Re = 250$ is given in figure 13. In both cases there is an absence of viscous dissipation or turbulent diffusion as demonstrated in figure 9 and the total pressure is conserved through the fountain height. The higher centreline momentum flux of the parabolic profile means the fountain reaches a greater height. The convergence of the two profiles at lower Froude numbers to $z_m = 1.26Fr^{2/3}$ in figure 8 is indicative of the transition to the hydraulically controlled very weak flow regime.

This result may explain some of the scatter in the range $Fr = 1.0$–3.0 in figure 8. The higher Reynolds number simulations in this study at $Fr = 0.97$, 1.4 and 2.1 coincide well with Zhang & Baddour (1998) but the penetration heights are greater than the uniform axisymmetric simulations of Lin & Armfield (2000*a*) in this region.

7. Conclusions

Turbulent weak fountain flow has been examined over the range $Fr = 0.1$–2.1. The scaling for the fountain height, the initial rise time behaviour and momentum balances have shown that there is a continuum of behaviour over this transition Froude number range, from hydraulically driven buoyancy dominated flow to momentum dominated flow. The absence of energy dissipation in this flow enables the fountain penetration height to be described using a simple hydraulic energy balance, $z_m = 1/2\, u^2 Fr^2 + (p_0 - p_t)Fr^2$.

For $Fr < 0.4$ and $Re > 250$, the flow is dominated by $(p_0 - p_t)Fr^2$ and the fountain height rises to provide a radial pressure gradient which accelerates the fluid away from the fountain source radially. In this regime $z_m = A_1 Fr^{2/3} + A_2 Fr^{2/3}$. The $A_1 Fr^{2/3}$ term represents the scaling of the radial pressure gradient. In very weak wall-bounded fountain flow, the intrusion is directly connected with the fountain outflow. Backpressure from the outflow increases the required fountain penetration height and this is represented in the second term in the scaling ($A_2 Fr^{2/3}$). The viscous effects at the source are small for $Re > 250$. For $Re \lesssim 100$ the radial outflow is at a subcritical Froude number everywhere and the flow behaves as a viscous gravity current.

Over the transition range of $Fr = 0.4$–2.1, the flow rises with two regions having distinct behaviours, an upflow core where the height correlates with $h_2 \approx 1/2(uFr)^2$ and a cap region where very weak flow behaviour is observed. The combined scaling can be given as $z_m \sim C_1 Fr^{2/3} + C_2 Fr^2$. Over this transition range the effect of source velocity profile is more significant than Reynolds number effects.

The authors acknowledge the support of the Australian Research Council.

Supplementary movies available at journals.cambridge.org/flm.

REFERENCES

Armfield, S. W. & Street, R. 1999 The fractional step method for the Navier–Stokes equations on staggered grids: The accuracy of three variations. *J. Comput. Phys.* **153**, 660–665.

Armfield, S. W. & Street, R. 2002 An analysis and comparison of the time accuracy of fractional-step methods for the Navier–Stokes equations on staggered grids. *Intl J. Numer. Meth. Fluids* **38**, 255–282.

Baddour, R. E. & Zhang, H. 2009 Density effect on round turbulent hypersaline fountain. *J. Hydraul. Engng* **135**, 57–59.

Baines, W. D., Turner, J. S. & Campbell, I. H. 1990 Turbulent fountains in an open chamber. *J. Fluid Mech.* **212**, 557–592.

Bloomfield, L. J. & Kerr, R. C. 1998 Turbulent fountains in a stratified fluid. *J. Fluid Mech.* **358**, 335–356.

Bloomfield, L. J. & Kerr, R. C. 2000 A theoretical model of a turbulent fountain. *J. Fluid Mech.* **424**, 197–216.

Brandt, A. 1977 Multi-level adaptive solutions to boundary-value problems. *Math. Comput.* **31** (138), 333–390.

Campbell, I. H. & Turner, J. S. 1989 Fountains in magma chambers. *J. Petrol.* **30**, 885–923.

Cresswell, R. W. & Szczepura, R. T. 1993 Experimental investigation into a turbulent jet with negative buoyancy. *Phys. Fluids* A **5**, 2865–2878.

van der Vorst, H. A. 1992 Bi-CGSTAB: A fast and smoothly converging variant of Bi-CG for the solution of nonsymmetric linear systems. *SIAM J. Sci. Stat. Comput.* **13** (2), 631–644.

Fukagata, K. & Kasagi, N. 2002 Highly energy-conservative finite difference method for the cylindrical coordinate system. *J. Comput. Phys.* **181**, 478–498.

Huppert, H. E. 1982 The propagation of two-dimensional and axisymmetric viscous gravity currents over a rigid horizontal surface. *J. Fluid Mech.* **121**, 43–58.

Kaye, N. B. & Hunt, G. R. 2006 Weak fountains. *J. Fluid Mech.* **558**, 319–328.

Leonard, B. P. & Mokhtari, S. 1990 Beyond first-order upwinding: The ultra-sharp alternative for non-oscillatory steady state simulation of convection. *Intl J. Numer. Meth. Engng* **30**, 729–766.

Lin, W. & Armfield, S. W. 2000*a* Direct simulation of weak axisymmetric fountains in a homogeneous fluid. *J. Fluid Mech.* **403**, 67–88.

Lin, W. & Armfield, S. W. 2000*b* Very weak axisymmetric fountains in a homogeneous fluid. *Numer. Heat Transfer* A **38**, 377–396.

Lin, W. & Armfield, S. W. 2003 The Reynolds and Prandtl number dependence of weak fountains. *Comput. Mech.* **31**, 379–389.

Mizushina, T., Ogino, F., Takeuchi, H. & Ikawa, H. 1982 An experimental study of vertical turbulent jet with negative buoyancy. *Wärme-und Stoffübertragung* **16**, 15–21.

Pantzlaff, L. & Lueptow, R. M. 1999 Transient positively and negatively buoyant turbulent round jets. *Exp. Fluids* **27**, 117–125.

Snyder, D. & Tait, S. 1995 Replenishment of magma chambers: comparison of fluid-mechanic experiments with field relations. *Contrib. Mineral Petrol.* **122**, 230–240.

Turner, J. S. 1966 Jets and plumes with negative or reversing buoyancy. *J. Fluid Mech.* **26**, 779–792.

Williamson, N., Armfield, S. W. & Lin, W. 2008*a* Direct numerical simulation of turbulent intermediate Froude number fountain flow. *ANZIAM J.* **50**, C16–C30.

Williamson, N., Srinarayana, N., Armfield, S. W., McBain, G. D. & Lin, W. 2008*b* Low-Reynolds-number fountain behaviour. *J. Fluid Mech.* **608**, 297–317.

Zhang, H. & Baddour, R. E. 1997 Maximum vertical penetration of plane turbulent negatively buoyant jets. *J. Engng Mech.* **123**, 973–977.

Zhang, H. & Baddour, R. E. 1998 Maximum penetration of vertical round dense jets at small and large Froude numbers. *J. Hydraul. Engng* **124**, 550–553.